IAC–22–C1,4,8,x69397

Hardware-in-the-loop Proximity Operations in Cislunar Space

Vivek Muralidharan[a], Mohatashem Reyaz Makhdoomi[a], Kuldeep Rambhai Barad[a], Lina María Amaya-Mejía[a], Kathleen C. Howell[b], Carol Martinez[a], and Miguel Olivares-Mendez[a]

[a] Space Robotics Research Group, SnT - University of Luxembourg, 1855 Luxembourg
{vivek.muralidharan, mohatashem.makhdoomi, kuldeep.barad}@uni.lu,
lina.amaya.001@student.uni.lu, {carol.martinezluna, miguel.olivaresmendez}@uni.lu

[b] School of Aeronautics and Astronautics, Purdue University, West Lafayette, IN 47907, USA,
howell@purdue.edu

Space missions to Near Rectilinear Halo Orbits (NRHOs) in the Earth-Moon system are upcoming. A rendezvous technique in the cislunar space is proposed in this investigation, one that leverages coupled orbit and attitude dynamics in the Circular Restricted Three-body Problem (CR3BP). An autonomous Guidance, Navigation and Control (GNC) technique is demonstrated in which a chaser spacecraft approaches a target spacecraft in the southern 9:2 synodic-resonant L2 Near Rectilinear Halo Orbit (NRHO), one that currently serves as the baseline for NASA's Gateway. A two-layer control approach is contemplated. First, a nonlinear optimal controller identifies an appropriate baseline rendezvous path, both in position and orientation. As the spacecraft progresses along the pre-computed baseline path, optical sensors measure the relative pose of the chaser relative to the target. A Kalman filter processes these observations and offers precise state estimates. A linear controller compensates for any deviations identified from the predetermined rendezvous path. The efficacy of the GNC technique is tested by considering a complex scenario in which the rendezvous operation is conducted with a non-cooperative tumbling target. Hardware-in-the-loop laboratory experiments are conducted as proof-of-concept to validate the guidance algorithm, with observations supplemented by optical navigation techniques.

1. Introduction

NASA's Gateway mission is being developed as a long-term hub, that potentially includes humans on board and offers logistical support for various future missions.[1] Cargo delivery and refueling modules are expected to transport necessary life-support systems for the crew as well as an exchange of essential pressurized and unpressurized cargo, science experiments supply, fuel, and advanced external robotics equipment. The facility contains several docking ports for visiting vehicles and future modules, as well as space for science and stowage.[2] Considering such operations becoming ubiquitous, precise rendezvous and docking techniques become essential for the longevity of the Gateway facility.

Guidance, Navigation and control (GNC) technique for proximity operations is the focus of this investigation. A coupled orbit and attitude dynamics in the Circular Restricted Three-body Problem (CR3BP) is leveraged to achieve close proximity operations.[3] The target body is assumed to be stationed along the 9:2 synodic resonant southern L2 NRHO in the Earth-Moon system, the current baseline for the Gateway. The target spacecraft however is considered passive and does not have active controllers for orbit and attitude control. Only the chaser spacecraft has the ability to deliver control maneuvers during the rendezvous process. Both the target and the chaser spacecrafts are influenced by the gravitational forces exerted by the Earth and Moon. A two-layered control approach is formulated for the proximity operations.[4] Firstly, a nonlinear controller using the Interior-Point Optimization (IPOPT) technique identifies a baseline approach path, in both position and orientation. Subsequently, any deviations identified from this predetermined baseline are overcome by a linear controller. Optical instruments capture the relative pose at regular intervals as the chaser spacecraft progresses toward the target. A Kalman filter is incorporated to deliver precise state estimates despite uncertainties and fluctuations in pose observations and run in sync with the control algorithm.[5]

The proposed guidance and control algorithm is tested via hardware-in-the-loop experiments in the ZeroG-Lab facility at the University of Luxembourg. Scaled mockups of CubeSats are mounted on the end-

effectors of two robotic manipulators, and the trajectory and attitude motion in the cislunar environment are simulated. Further, optical sensors mounted on the chaser spacecraft, in form of a monocular camera, detect semantic features on the target spacecraft in real-time. Using the correspondence of the detected key points in the known wireframe model of the target, an Efficient Perspective-n-Point (EPnP) solver estimates the relative pose of the target. A closed-loop test is conducted with a tumbling target to validate the architecture. The hardware experiments offer proof-of-concept for leveraging optical measurements for rendezvous planning in deep space environments.

2. Dynamics

2.1 Circular Restricted Three-Body Problem

A rendezvous scenario is considered for a cislunar mission. The trajectory and the attitude dynamics are influenced primarily by the two main gravitational forces, due to the Earth and the Moon. The circular restricted three-body problem (CR3BP) offers a time invariant approximation for the spacecraft dynamics in the higher-fidelity model. The motion of a spacecraft in the CR3BP model is influenced by the gravitational forces of the Earth and the Moon, assumed to be rotating in coplanar circular orbits about their mutual barycenter, O.[6] A synodic frame [S] is thus defined as

$$[\mathrm{S}] = \{\mathrm{O\ (Barycenter)}: \quad \hat{i}_{[\mathrm{S}]}, \hat{j}_{[\mathrm{S}]}, \hat{k}_{[\mathrm{S}]}\}$$

and rotates about the inertial frame [I] at a rate consistent with the angular rate of revolution of the Earth and Moon. Unit vector $\hat{i}_{[\mathrm{S}]}$ points from the Earth towards the Moon, $\hat{k}_{[\mathrm{S}]}$ is along the positive orbital angular momemtum direction, and finally, $\hat{j}_{[\mathrm{S}]}$ completes the dextral coordinate system. The inertial frame,

$$[\mathrm{I}] = \{\mathrm{O\ (Barycenter)}: \quad \hat{i}_{[\mathrm{I}]}, \hat{j}_{[\mathrm{I}]}, \hat{k}_{[\mathrm{I}]}\}$$

shares the same origin as the [S] frame. Figure 1 offers a schematic representation of the different coordinate frames used in this investigation. By convention, the dynamical equations of motion for the spacecraft in the CR3BP is modelled in the synodic frame [S], with the position and the velocity quantities non-dimensionalized using characteristics quantities. In the Earth-Moon system, Earth is the primary body P1 while P2 represents the Moon. In the Earth-Moon system, the characteristic length, l^*, is defined as the mean distance between the Earth and the Moon, while the characteristic time, t^*, is defined as the reciprocal of their mean motion about their barycenter. The values for the characteristics quantities are approximately, $l^* \approx 385692.50$ km and $t^* \approx 377084.15$ seconds.[7] Since the orbit of interest is in close proximity of the Moon, a Moon centered rotating frame [M] is also defined,

$$[\mathrm{M}] = \{\mathrm{Moon}: \quad \hat{i}_{[\mathrm{M}]}, \hat{j}_{[\mathrm{M}]}, \hat{k}_{[\mathrm{M}]}\}$$

and offers a direct linear translation from the [S] frame, such that,

$$x_{[\mathrm{M}]} = (1-\mu) - x_{[\mathrm{S}]} \quad [1]$$

$$y_{[\mathrm{M}]} = -y_{[\mathrm{S}]} \quad [2]$$

$$z_{[\mathrm{M}]} = z_{[\mathrm{S}]} \quad [3]$$

where μ is the system mass ratio, defined as the ratio of the mass of P2 to the overall mass of the system, i.e., $\mu = m_2/(m_1+m_2)$, where m_1 and m_2 are the masses of bodies P1 and P2, respectively. The equations of motion for the spacecraft in the [M] frame is governed by

$$\ddot{x}_{[\mathrm{M}]} - 2\dot{y}_{[\mathrm{M}]} - x_{[\mathrm{M}]} = -\frac{1-\mu}{d_1^3}(x_{[\mathrm{M}]}-1) - \frac{\mu}{d_2^3}x_{[\mathrm{M}]} - (1-\mu) \quad [4]$$

$$\ddot{y}_{[\mathrm{M}]} + 2\dot{x}_{[\mathrm{M}]} - y_{[\mathrm{M}]} = -\frac{1-\mu}{d_1^3}y_{[\mathrm{M}]} - \frac{\mu}{d_2^3}y_{[\mathrm{M}]} \quad [5]$$

$$\ddot{z}_{[\mathrm{M}]} = -\frac{1-\mu}{d_1^3}z_{[\mathrm{M}]} - \frac{\mu}{d_2^3}z_{[\mathrm{M}]} \quad [6]$$

where the quantities d_1 and d_2,

$$d_1 = \sqrt{(x_{[\mathrm{M}]}-1)^2 + y_{[\mathrm{M}]}^2 + z_{[\mathrm{M}]}^2} \quad [7]$$

$$d_2 = \sqrt{x_{[\mathrm{M}]}^2 + y_{[\mathrm{M}]}^2 + z_{[\mathrm{M}]}^2} \quad [8]$$

are the scalar non-dimensional distance from the target spacecraft to the primary bodies P1 and P2, respectively.

2.2 Relative Motion

The relative motion between a chaser and a target spacecraft offers detailed insight, especially in a close proximity operations such as rendezvous. A coordinate frame centered on the target spacecraft is appropriate to realize the relative motion. A Local Velocity Local Horizon (LVLH) frame is defined as,

$$[\mathrm{L}] = \{\mathrm{Target\ spacecraft}: \quad \hat{i}_{[\mathrm{L}]}, \hat{j}_{[\mathrm{L}]}, \hat{k}_{[\mathrm{L}]}\}$$

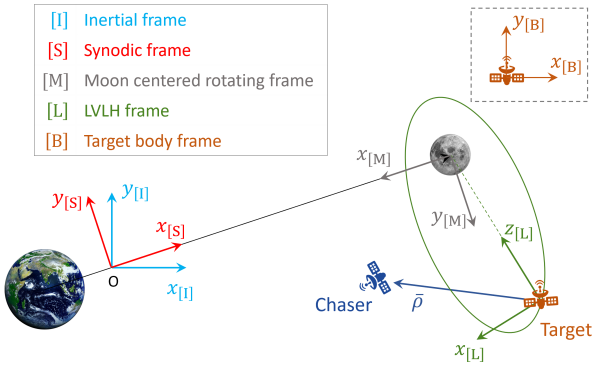

Fig. 1: Coordinate frames for spacecraft motion

where positive $\hat{k}_{[\mathrm{L}]}$ is in the direction from the target spacecraft to the central body, i.e., the Moon. The direction away from the orbital angular momentum is given by positive $\hat{j}_{[\mathrm{L}]}$ direction. Finally, $\hat{i}_{[\mathrm{L}]}$ completes the right-hand coordinate system. Mathematically, these directions are derived as

$$\hat{k}_{[\mathrm{L}]} = -\frac{\mathbf{r}}{||\mathbf{r}||}\ ,\quad \hat{j}_{[\mathrm{L}]} = -\frac{\mathbf{h}}{||\mathbf{h}||}\ ,\quad \hat{i}_{[\mathrm{L}]} = \hat{j}_{[\mathrm{L}]} \times \hat{k}_{[\mathrm{L}]} \quad [9]$$

where $\mathbf{r}$ represents the target position vector from the central body, i.e., the Moon. Expressed in the Moon centered rotating frame, $\mathbf{r}$ is equivalent to $\bar{r}_{[\mathrm{M}]}$.

$$\bar{r}_{[\mathrm{M}]} = [x_{[\mathrm{M}]}, y_{[\mathrm{M}]}, z_{[\mathrm{M}]}]^{\mathrm{T}} \quad [10]$$

where, superscript 'T' indicates a transpose. Similarly, $\mathbf{h}$ is the instantaneous orbital angular momentum vector, i.e., $\mathbf{h} = \mathbf{r} \times \mathbf{v}$; note that, $\mathbf{v}$ is the target velocity relative to the central body. In the Moon centered rotating frame, $\mathbf{v} = \dot{\bar{r}}_{[\mathrm{M}]}$. The directions, $\hat{i}_{[\mathrm{L}]}, \hat{j}_{[\mathrm{L}]}$ and $\hat{k}_{[\mathrm{L}]}$ are sometimes referred as V-bar, H-bar, and R-bar directions, respectively.[8]

The relative equations of motion for the chaser relative to the target are derived as a difference of the gravitational acceleration experienced by each of the spacecrafts. Applying Newton's laws for universal gravitation, the acceleration for the target spacecraft is governed by,

$$\ddot{\mathbf{r}}_{[\mathrm{I}]} = -\mu\frac{\mathbf{r}}{||\mathbf{r}||^3} - (1-\mu)\left(\frac{\mathbf{r}+\mathbf{r}_{em}}{||\mathbf{r}+\mathbf{r}_{em}||^3} - \frac{\mathbf{r}_{em}}{||\mathbf{r}_{em}||^3}\right) \quad [11]$$

while the acceleration due to gravitational forces experienced by the chaser is given by,

$$\ddot{\mathbf{r}}_{c[\mathrm{I}]} = -\mu\frac{\mathbf{r}_c}{||\mathbf{r}_c||^3} - (1-\mu)\left(\frac{\mathbf{r}_c+\mathbf{r}_{em}}{||\mathbf{r}_c+\mathbf{r}_{em}||^3} - \frac{\mathbf{r}_{em}}{||\mathbf{r}_{em}||^3}\right) \quad [12]$$

where $\mathbf{r}_c$ is the chaser position vector from the the central body, the Moon. The position of the chaser relative to the target, i.e., $\bar{\rho}$, is the difference between the position vector of the chaser and the target,

$$\bar{\rho} = \mathbf{r}_c - \mathbf{r} \quad [13]$$

and the evolution of such a quantity is the basis for any proximity operations. Using the basic kinematic equation the velocity and the acceleration of the chaser spacecraft in the inertial frame, i.e.,

$$\dot{\mathbf{r}}_{c[\mathrm{I}]} = \dot{\mathbf{r}}_{[\mathrm{I}]} + \dot{\bar{\rho}}_{[\mathrm{I}]} = \dot{\mathbf{r}}_{[\mathrm{I}]} + \dot{\bar{\rho}}_{[\mathrm{L}]} + \omega_{\mathrm{L/I}} \times \bar{\rho}_{[\mathrm{L}]} \quad [14]$$

$$\ddot{\mathbf{r}}_{c[\mathrm{I}]} = \ddot{\mathbf{r}}_{[\mathrm{I}]} + \ddot{\bar{\rho}}_{[\mathrm{L}]} + 2\omega_{\mathrm{L/I}} \times \dot{\bar{\rho}}_{[\mathrm{L}]} + \dot{\omega}_{\mathrm{L/I}} \times \bar{\rho}_{[\mathrm{L}]} + \omega_{\mathrm{L/I}} \times (\omega_{\mathrm{L/I}} \times \bar{\rho}_{[\mathrm{L}]}) \quad [15]$$

are expressed as a function of the relative position in the LVLH frame, $\bar{\rho}_{[\mathrm{L}]}$, as well as the angular velocity ($\omega_{\mathrm{L/I}}$) and angular acceleration ($\dot{\omega}_{\mathrm{L/I}}$). Moreover, the subscript L/I represents frame transformation from LVLH frame [L] to the inertial frame [I]. Note that, similar subscripts are defined to represent other frame transformations. Substituting equations [11] and [12] into equation [15], the higher order time derivatives for $\bar{\rho}_{[\mathrm{L}]}$ are determined as the functions of itself. The updated equation,

$$\begin{aligned}\ddot{\bar{\rho}}_{[\mathrm{L}]} =& -2\omega_{\mathrm{L/I}} \times \dot{\bar{\rho}}_{[\mathrm{L}]} - \dot{\omega}_{\mathrm{L/I}} \times \bar{\rho}_{[\mathrm{L}]} \\ & - \omega_{\mathrm{L/I}} \times (\omega_{\mathrm{L/I}} \times \bar{\rho}_{[\mathrm{L}]}) \\ & - \mu\frac{\mathbf{r}_c}{||\mathbf{r}_c||^3} - (1-\mu)\left(\frac{\mathbf{r}_c+\mathbf{r}_{em}}{||\mathbf{r}_c+\mathbf{r}_{em}||^3} - \frac{\mathbf{r}_{em}}{||\mathbf{r}_{em}||^3}\right) \\ & + \mu\frac{\mathbf{r}}{||\mathbf{r}||^3} + (1-\mu)\left(\frac{\mathbf{r}+\mathbf{r}_{em}}{||\mathbf{r}+\mathbf{r}_{em}||^3} - \frac{\mathbf{r}_{em}}{||\mathbf{r}_{em}||^3}\right)\end{aligned} \quad [16]$$

describes the nonlinear equations for relative motion in the restricted three-body problem.[9,10] The angular velocity and the angular acceleration for frame [L] relative to the inertial frame [I] is expressed as a combination of frame rotation from LVLH to Moon centered rotating frame ([L] → [M]) and from Moon centered rotating frame to the inertial frame ([M] → [I]), such that

$$\omega_{\mathrm{L/I}} = \omega_{\mathrm{L/M}} + \omega_{\mathrm{M/I}} \quad [17]$$

$$\dot{\omega}_{\mathrm{L/I[L]}} = \dot{\omega}_{\mathrm{L/M}} + \dot{\omega}_{\mathrm{M/I[M]}} - \omega_{\mathrm{L/M}} \times \omega_{\mathrm{M/I}} \quad [18]$$

and employs the following relationships,

$$\omega_{\mathrm{L/M[L]}} = \omega^x_{\mathrm{L/M}}\hat{i}_{[\mathrm{L}]} + \omega^y_{\mathrm{L/M}}\hat{j}_{[\mathrm{L}]} + \omega^z_{\mathrm{L/M}}\hat{k}_{[\mathrm{L}]} \quad [19]$$

$$\omega^x_{\mathrm{L/M}} = 0 \quad [20]$$

$$\omega^y_{\mathrm{L/M}} = -\frac{||\mathbf{h}||}{||\mathbf{r}||^2} \quad [21]$$

$$\omega^z_{\mathrm{L/M}} = -\frac{||\mathbf{r}||}{||\mathbf{h}||^2}\ \mathbf{h}\cdot\ddot{\bar{r}}_{[\mathrm{M}]} \quad [22]$$

that correspond to instantaneous values for angular rotations resulting from frame transformations. The frame transformation, [L] → [M], is a characteristic of the motion of the target body around the Moon while the frame transformation, [M] → [I] is symbolic of the rotation of primary bodies, particularly the Moon around the barycenter. Using the simplifying assumptions in the CR3BP model, $\omega_{\mathrm{M/I}} = \hat{k}_{[\mathrm{M}]}$ is fixed; as a consequence, $\dot{\omega}_{\mathrm{M/I}} = 0$. The quantity $\ddot{\bar{r}}_{[\mathrm{M}]}$, such that, $\ddot{\bar{r}}_{[\mathrm{M}]} = [\ddot{x}_{[\mathrm{M}]}, \ddot{y}_{[\mathrm{M}]}, \ddot{z}_{[\mathrm{M}]}]^{\mathrm{T}}$, is as determined in equations [4], [5] and [6]. Similarly,

$$\dot{\omega}_{\mathrm{L/M[L]}} = \dot{\omega}^x_{\mathrm{L/M}}\hat{i}_{[\mathrm{L}]} + \dot{\omega}^y_{\mathrm{L/M}}\hat{j}_{[\mathrm{L}]} + \dot{\omega}^z_{\mathrm{L/M}}\hat{k}_{[\mathrm{L}]} \quad [23]$$

$$\dot{\omega}^x_{\mathrm{L/M}} = 0 \quad [24]$$

$$\dot{\omega}^y_{\mathrm{L/M}} = -\frac{1}{||\mathbf{r}||}\left(\frac{\dot{h}}{||\mathbf{r}||} + 2\dot{r}\omega^y_{\mathrm{L/M}}\right) \quad [25]$$

$$\dot{\omega}^z_{\mathrm{L/M}} = \left(\frac{\dot{r}}{||\mathbf{r}||} - 2\frac{\dot{h}}{||\mathbf{h}||}\right)\omega^z_{\mathrm{L/M}} - \frac{||\mathbf{r}||}{||\mathbf{h}||^2}\ \mathbf{h}\cdot\dddot{\bar{r}}_{\ [\mathrm{M}]} \quad [26]$$

where the following relationships apply,

$$\dot{h} = -\dot{\mathbf{h}}_{[\mathrm{M}]}\cdot\hat{j} \quad [27]$$

$$\dot{r} = \frac{1}{||\mathbf{r}||}\bar{r}_{[\mathrm{M}]}\cdot\dot{\bar{r}}_{[\mathrm{M}]} \quad [28]$$

including the jerk experienced by the target body in the [M] frame,

$$\begin{aligned}\dddot{\bar{r}}_{\ [\mathrm{M}]} =& -2\omega_{\mathrm{M/I}}\times\ddot{\bar{r}}_{[\mathrm{M}]} - \omega_{\mathrm{M/I}}\times(\omega_{\mathrm{M/I}}\times\dot{\bar{r}}_{[\mathrm{M}]}) \\ &- (1-\mu)\frac{\partial}{\partial\mathbf{r}}\left[\frac{\mathbf{r}+\mathbf{r}_{em}}{||\mathbf{r}+\mathbf{r}_{em}||^3}\right]\dot{\bar{r}}_{[\mathrm{M}]} \\ &- \mu\frac{\partial}{\partial\mathbf{r}}\left[\frac{\mathbf{r}}{||\mathbf{r}||^3}\right]\dot{\bar{r}}_{[\mathrm{M}]}\end{aligned} \quad [29]$$

where, the following rule for differentiation applies,

$$\frac{\partial}{\partial\mathbf{q}}\left[\frac{\mathbf{q}}{||\mathbf{q}||^3}\right] = \frac{1}{||\mathbf{q}||^3}\left(\mathbf{I} - 3\frac{\mathbf{q}\mathbf{q}^{\mathrm{T}}}{||\mathbf{q}||^2}\right) \quad [30]$$

for any vector $\mathbf{q}$. The analytical solutions for relative motion of the chaser relative to the target are not available and thus the system dynamics are contemplated through numerical integration.

In a rendezvous scenario, the motion of the chaser spacecraft is not only governed by the natural dynamics but also the additional acceleration employed by the thrusters on the chaser spacecraft. These acceleration components serve as the control parameter that is varied to achieve rendezvous. On modifying equation [16] along with additional acceleration control parameters u_1, u_2, u_3, the relative acceleration of the chaser relative to the target is formulated as

$$\begin{aligned}\ddot{\bar{\rho}}_{[\mathrm{L}]} =& -2\Omega_{\mathrm{L/I[L]}}\dot{\bar{\rho}}_{[\mathrm{L}]} - (\dot{\Omega}_{\mathrm{L/I[L]}} + \Omega^2_{\mathrm{L/I[L]}})\bar{\rho}_{[\mathrm{L}]} \\ &(1-\mu)\left(\frac{\mathbf{r}+\mathbf{r}_{em}}{||\mathbf{r}+\mathbf{r}_{em}||^3} - \frac{\mathbf{r}+\bar{\rho}+\mathbf{r}_{em}}{||\mathbf{r}+\bar{\rho}+\mathbf{r}_{em}||^3}\right) \\ &+ \mu\left(\frac{\mathbf{r}}{||\mathbf{r}||^3} - \frac{\mathbf{r}+\bar{\rho}}{||\mathbf{r}+\bar{\rho}||^3}\right) + [u_1, u_2, u_3]^{\mathrm{T}}\end{aligned} \quad [31]$$

where the following relation holds,

$$\Omega_{\mathrm{L/I\ [L]}} = \begin{bmatrix} 0 & -\omega^z_{\mathrm{L/I}} & \omega^y_{\mathrm{L/I}} \\ \omega^z_{\mathrm{L/I}} & 0 & -\omega^x_{\mathrm{L/I}} \\ -\omega^y_{\mathrm{L/I}} & \omega^x_{\mathrm{L/I}} & 0 \end{bmatrix} \quad [32]$$

$$\dot{\Omega}_{\mathrm{L/I\ [L]}} = \begin{bmatrix} 0 & -\dot{\omega}^z_{\mathrm{L/I}} & \dot{\omega}^y_{\mathrm{L/I}} \\ \dot{\omega}^z_{\mathrm{L/I}} & 0 & -\dot{\omega}^x_{\mathrm{L/I}} \\ -\dot{\omega}^y_{\mathrm{L/I}} & \dot{\omega}^x_{\mathrm{L/I}} & 0 \end{bmatrix} \quad [33]$$

$$\omega_{\mathrm{L/I\ [L]}} = \omega^x_{\mathrm{L/I}}\hat{i}_{[\mathrm{L}]} + \omega^y_{\mathrm{L/I}}\hat{j}_{[\mathrm{L}]} + \omega^z_{\mathrm{L/I}}\hat{k}_{[\mathrm{L}]} \quad [34]$$

$$\dot{\omega}_{\mathrm{L/I\ [L]}} = \dot{\omega}^x_{\mathrm{L/I}}\hat{i}_{[\mathrm{L}]} + \dot{\omega}^y_{\mathrm{L/I}}\hat{j}_{[\mathrm{L}]} + \dot{\omega}^z_{\mathrm{L/I}}\hat{k}_{[\mathrm{L}]} \quad [35]$$

and these equations are numerically integrated to identify the relative position for the chaser in the LVLH frame [L] such that

$$\bar{\rho}_{[\mathrm{L}]} = \rho_x\hat{i}_{[\mathrm{L}]} + \rho_y\hat{j}_{[\mathrm{L}]} + \rho_z\hat{k}_{[\mathrm{L}]} \quad [36]$$

where ρ_x, ρ_y and ρ_z are the projections of the position vector along each of the $\hat{i}_{[\mathrm{L}]}$, $\hat{j}_{[\mathrm{L}]}$ and $\hat{k}_{[\mathrm{L}]}$ directions, respectively. Such quantities in the [L] frame are also appropriate for simulating close proximity operations in a laboratory environment.

2.3 Attitude Dynamics

During the phase of a rendezvous operation, where the relative distance between the chaser and the target is significantly high, the actual relative orientation of the bodies are trivial. However, during the final rendezvous phase such as docking, the relative orientation of these bodies are crucial. During rendezvous, the chaser spacecraft is expected to be aligned in a particular configuration relative to the body frame of the target spacecraft. Consistently, the attitude dynamics for the chaser is modelled relative to the target body. Employing Euler's equations of motion to reflect the rotational dynamics of

the spacecraft, the quantities for angular velocity are expressed as

$$ {}^{C}\dot{\omega_1} = \frac{1}{{}^{C}I_1}\left(T_1 - \left({}^{C}I_3 - {}^{C}I_2\right){}^{C}\omega_2{}^{C}\omega_3\right) \quad [37] $$

$$ {}^{C}\dot{\omega_2} = \frac{1}{{}^{C}I_2}\left(T_2 - \left({}^{C}I_1 - {}^{C}I_3\right){}^{C}\omega_1{}^{C}\omega_3\right) \quad [38] $$

$$ {}^{C}\dot{\omega_3} = \frac{1}{{}^{C}I_3}\left(T_3 - \left({}^{C}I_2 - {}^{C}I_1\right){}^{C}\omega_1{}^{C}\omega_2\right) \quad [39] $$

where ${}^{C}\omega \equiv \omega(Chaser \rightarrow Target)$ and ${}^{C}\epsilon_i \equiv \epsilon_i(Chaser \rightarrow Target)$ with a left superscript, C. The moment of inertia for the chaser along each of its principal axis are given by ${}^{C}I_j$, with $j = 1, 2, 3$. The quantities T_1, T_2 and T_3 are components that include external torques experienced by the chaser. The attitude of the chaser is stabilized as desired by controlling the values for T_1, T_2 and T_3. The instantaneous orientation of the chaser body relative to the target body are expressed in terms of rotation quaternions

$$ {}^{C}\dot{\epsilon_1} = \frac{1}{2}\left({}^{C}\omega_1{}^{C}\epsilon_4 - {}^{C}\omega_2{}^{C}\epsilon_3 + {}^{C}\omega_3{}^{C}\epsilon_2\right) \quad [40] $$

$$ {}^{C}\dot{\epsilon_2} = \frac{1}{2}\left({}^{C}\omega_1{}^{C}\epsilon_3 + {}^{C}\omega_2{}^{C}\epsilon_4 - {}^{C}\omega_3{}^{C}\epsilon_1\right) \quad [41] $$

$$ {}^{C}\dot{\epsilon_3} = \frac{1}{2}\left(-{}^{C}\omega_1{}^{C}\epsilon_2 + {}^{C}\omega_2{}^{C}\epsilon_1 + {}^{C}\omega_3{}^{C}\epsilon_4\right) \quad [42] $$

$$ {}^{C}\dot{\epsilon_4} = \frac{1}{2}\left(-{}^{C}\omega_1{}^{C}\epsilon_1 - {}^{C}\omega_2{}^{C}\epsilon_2 - {}^{C}\omega_3{}^{C}\epsilon_3\right) \quad [43] $$

where ϵ_1, ϵ_2 and ϵ_3 offer insight into the orientation of the axis of rotation while ϵ_4 shadow the degree of spin about the axis of rotation. Also $\epsilon_1^2 + \epsilon_2^2 + \epsilon_3^2 + \epsilon_4^2 = 1$. The dynamics of the target body are, however, expressed relative to the inertial frame. Notations for the angular velocity and orientation quaternions are expressed with a left superscript, T, for example, ${}^{T}\omega \equiv \omega(Target \rightarrow Inertial)$. The target body is modelled such that the gravity torque affects its motion, such that

$$ {}^{T}\dot{\omega_1} = \frac{{}^{T}I_3 - {}^{T}I_2}{{}^{T}I_1}\left(3\frac{1-\mu}{d_1^5}g_2g_3 + 3\frac{\mu}{d_2^5}h_2h_3 - {}^{T}\omega_2{}^{T}\omega_3\right) \quad [44] $$

$$ {}^{T}\dot{\omega_2} = \frac{{}^{T}I_1 - {}^{T}I_3}{{}^{T}I_2}\left(3\frac{1-\mu}{d_1^5}g_1g_3 + 3\frac{\mu}{d_2^5}h_1h_3 - {}^{T}\omega_1{}^{T}\omega_3\right) \quad [45] $$

$$ {}^{T}\dot{\omega_3} = \frac{{}^{T}I_2 - {}^{T}I_1}{{}^{T}I_3}\left(3\frac{1-\mu}{d_1^5}g_1g_2 + 3\frac{\mu}{d_2^5}h_1h_2 - {}^{T}\omega_1{}^{T}\omega_2\right) \quad [46] $$

where the terms including $(1-\mu)$ quantify the effects of gravity torque due to body P1, i.e., the Earth; while terms including μ are associated with the gravity gradient torque exerted by body P2, i.e., the Moon.[3,11] Similarly, the equations for the quaternions

$$ {}^{T}\dot{\epsilon_1} = \frac{1}{2}\left({}^{T}\omega_1{}^{T}\epsilon_4 - {}^{T}\omega_2{}^{T}\epsilon_3 + {}^{T}\omega_3{}^{T}\epsilon_2\right) \quad [47] $$

$$ {}^{T}\dot{\epsilon_2} = \frac{1}{2}\left({}^{T}\omega_1{}^{T}\epsilon_3 + {}^{T}\omega_2{}^{T}\epsilon_4 - {}^{T}\omega_3{}^{T}\epsilon_1\right) \quad [48] $$

$$ {}^{T}\dot{\epsilon_3} = \frac{1}{2}\left(-{}^{T}\omega_1{}^{T}\epsilon_2 + {}^{T}\omega_2{}^{T}\epsilon_1 + {}^{T}\omega_3{}^{T}\epsilon_4\right) \quad [49] $$

$$ {}^{T}\dot{\epsilon_4} = \frac{1}{2}\left(-{}^{T}\omega_1{}^{T}\epsilon_1 - {}^{T}\omega_2{}^{T}\epsilon_2 - {}^{T}\omega_3{}^{T}\epsilon_3\right) \quad [50] $$

offer the instantaneous orientation of the target body axis relative to the inertial frame. The quantities g_j and h_j represent the projections of position vector to P1 and P2 on the target body frame respectively.[3,12]

The chaser and target spacecrafts are rigid bodies, and, therefore, during rendezvous, the chaser spacecraft must remain at a fixed distance from the center of the target body without colliding. Labelled as 'approach site,' such a location is stationary in the body fixed frame of the target, [B]. The coordinates of the approach site, however, is not fixed in the inertial frame [I], the Moon centered rotating frame [M] or the LVLH coordinate frame [L] due to continuous frame rotations. Since the target spacecraft may be observed as tumbling in another frame of interest, the approach site is rather an instantaneous 3-dimensional location, as illustrated in Fig. 2. In this investigation, the approach site is assumed as the location of the geometric center of the chaser spacecraft for convenience. Consider the coordinates of the approach site as

$$ \bar{\varrho}_{[\mathrm{B}]} = b_1\hat{i}_{[\mathrm{B}]} + b_2\hat{j}_{[\mathrm{B}]} + b_3\hat{k}_{[\mathrm{B}]} $$

measured in the target body frame [B] defined by

$$ [\mathrm{B}] = \{\text{Target spacecraft}: \ \hat{i}_{[\mathrm{B}]}, \hat{j}_{[\mathrm{B}]}, \hat{k}_{[\mathrm{B}]}\} $$

that is centered on the target body and along its principal axes of inertia. Note that b_1, b_2 and b_3 are fixed parameters. The LVLH frame is however the working frame of view and offers direct understanding of the spacecraft's approach during the rendezvous process. With coordinate transformation, the approach site in the LVLH frame is represented as

$$ \bar{\varrho}_{[\mathrm{L}]} = \begin{pmatrix} \varrho_x \\ \varrho_y \\ \varrho_z \end{pmatrix} = {}^{[\mathrm{L}]}\mathbb{C}^{[\mathrm{B}]} \ \bar{\varrho}_{[\mathrm{B}]} = {}^{[\mathrm{L}]}\mathbb{C}^{[\mathrm{B}]}\begin{pmatrix} b_1 \\ b_2 \\ b_3 \end{pmatrix} $$

where ${}^{[\mathrm{L}]}\mathbb{C}^{[\mathrm{B}]} = \{\mathbb{C} : [\mathrm{B}] \rightarrow [\mathrm{L}]\}$ is the transformation matrix from target body frame [B] to the LVLH frame

[L]. The matrix ${}^{[\mathrm{L}]}\mathbb{C}^{[\mathrm{B}]}$,

$$ {}^{[\mathrm{L}]}\mathbb{C}^{[\mathrm{B}]} = {}^{[\mathrm{L}]}\mathbb{C}^{[\mathrm{M}]} \;\; {}^{[\mathrm{M}]}\mathbb{C}^{[\mathrm{I}]} \;\; {}^{[\mathrm{I}]}\mathbb{C}^{[\mathrm{B}]} \qquad [51] $$

is derived from a sequence of frame rotations, i.e., [B] $\rightarrow$ [I], [I] $\rightarrow$ [M] and finally [M] $\rightarrow$ [L]. The transformation matrix or the Direction Cosine Matrix (DCM), ${}^{[\mathrm{I}]}\mathbb{C}^{[\mathrm{B}]}$, is evaluated from the orientation quaternions, ${}^{T}\epsilon$. In the CR3BP model, $\omega_{\mathrm{M/I}} = \hat{k}_{[\mathrm{M}]}$ is fixed; as a consequence, the [M] frame rotates about the inertial frame [I] at a consistent rate proportional to the nondimensional time τ. Thus, enabling the computation of the transformation matrix ${}^{[\mathrm{M}]}\mathbb{C}^{[\mathrm{I}]}$. Finally, matrix ${}^{[\mathrm{L}]}\mathbb{C}^{[\mathrm{M}]}$ is determined from the correlations in equation [9].

During the rendezvous process, the chaser spacecraft progresses towards the approach site, $\bar{\rho}_{[\mathrm{L}]} \rightarrow \bar{\varrho}_{[\mathrm{L}]}$, i.e., $\rho_x \rightarrow \varrho_x$, $\rho_x \rightarrow \varrho_y$ and $\rho_z \rightarrow \varrho_z$. A chaser spacecraft may not necessarily dock along any particular principal axis of the target, therefore, leveraging the approach site while modelling the rendezvous process assists in defining complex docking scenario.

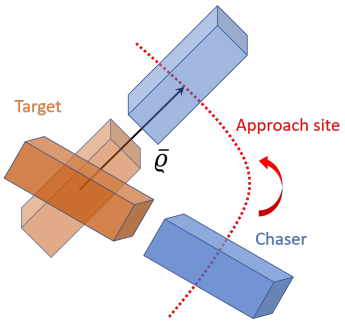

Fig. 2: Approach site, $\bar{\varrho}$, as a 3D location relative to the center of the target.[4]

3. Optimal Path Planning

The equations of motion for the trajectory and attitude dynamics are clearly nonlinear. For a successful rendezvous, a suitable path that drives the chaser towards the target is desired. Furthermore, both the chaser and target spacecrafts must have consistent orientation. A nonlinear control algorithm, CasADi, is introduced with the Interior Point Optimization (IPOPT) method to solve for an optimal path suitable for the proximity operations.[13] A cost functional, J, such that

$$ J = \int_0^{\tau} (\bar{\rho}_{[\mathrm{L}]} - \bar{\varrho}_{[\mathrm{L}]})^{\mathrm{T}} \mathbf{Q}_1 (\bar{\rho}_{[\mathrm{L}]} - \bar{\varrho}_{[\mathrm{L}]}) + {}^{C}\bar{\omega}^{\mathrm{T}} \mathbf{Q}_2 {}^{C}\bar{\omega} + {}^{C}\bar{\epsilon}^{\mathrm{T}} \mathbf{Q}_3 {}^{C}\bar{\epsilon} + \mathbf{u}^{\mathrm{T}} \mathbf{R} \mathbf{u} \;\; dt \qquad [52] $$

is minimized during the optimization process. Here weighting matrix $\mathbf{Q}_1$ penalizes any position deviation from the approach site, i.e., $\bar{\rho}_{[\mathrm{L}]} - \bar{\varrho}_{[\mathrm{L}]}$. The angular velocity of the chaser relative to the target is compensated by matrix $\mathbf{Q}_2$ whereas the relative difference in orientation between the two spacecrafts is penalized by matrix $\mathbf{Q}_3$. Finally, the control inputs $\mathbf{u}$ are weighted with matrix $\mathbf{R}$. The control input vector $\mathbf{u}_k$ is defined as,

$$ \mathbf{u}_k = [u_1, u_2, u_3, T_1, T_2, T_3]^{\mathrm{T}} $$

where u_1, u_2 and u_3 represent translational acceleration along each of the x, y and z directions in the [L] frame, respectively; T_1, T_2 and T_3 (also referred as u_4, u_5 and u_6) are the control torques that the chaser spacecraft may deliver. Each of the penalty matrices within the cost functional J may be updated for obtaining an alternate rendezvous path. An additional collision avoidance constraint is introduced such as

$$ ||\bar{\rho}|| \geq r_{collision} $$

to maintain the chaser spacecraft out of a spherical volume around the target spacecraft with a radius $r_{collision}$. The optimal states (both trajectory and attitude) obtained using the optimal control process serve as the baseline or the predicted reference path for rendezvous operations. The optimal path is an ideal path and does not account for any fluctuations or uncertainties in state estimation. Accordingly, state estimation and control algorithm are engaged in-sync throughout the entire rendezvous process.

4. Estimation and Linear Control

4.1 State Estimation

In close proximity, optical sensors typically on the chaser spacecraft determines the position and orientation vectors (also referred as "pose") of the target spacecraft, or perhaps any other target object including debris. Pose data are retrieved at discrete time intervals. Typical sensors are capable of capturing data at a frequency higher than 20 Hz. Raw observations may have large fluctuations and inherent uncertainties. Reacting upon individual observations and performing control maneuvers may destabilize the chaser spacecraft, incur large control costs and are trivial. Individual observed quantities are not a precise representation of the spacecraft states. Filtering techniques are therefore introduced to determine state variables with a reasonable precision. In the filtering process, a measurement matrix comprising of partials of observed state (pose in this case) with

respect to the state variables, are computed for every observations. Prior observations may be discarded in the case of a sequential Kalman filter thus offering advantage over a batch least squares filter in terms of computational memory allocation.[5,14] Consequently, a sequential Kalman filter is selected for this analysis.

System Dynamics

The chaser spacecraft principally evolves along a configuration predicted by the optimal controller to achieve rendezvous. Consider the configuration of the system described by the state vector $\mathbf{x}$,

$$\begin{aligned}\mathbf{x} =&[x_{[\mathrm{M}]}, y_{[\mathrm{M}]}, z_{[\mathrm{M}]}, \dot{x}_{[\mathrm{M}]}, \dot{y}_{[\mathrm{M}]}, \dot{z}_{[\mathrm{M}]},\\ &\rho_x, \rho_y, \rho_z, \dot{\rho_x}, \dot{\rho_y}, \dot{\rho_z},\\ &{}^{C}\omega_1, {}^{C}\omega_2, {}^{C}\omega_3, {}^{C}\epsilon_1, {}^{C}\epsilon_2, {}^{C}\epsilon_3, {}^{C}\epsilon_4,\\ &{}^{T}\omega_1, {}^{T}\omega_2, {}^{T}\omega_3, {}^{T}\epsilon_1, {}^{T}\epsilon_2, {}^{T}\epsilon_3, {}^{T}\epsilon_4, x_\varrho, y_\varrho, z_\varrho]^{\mathrm{T}}\end{aligned}$$

that captures information about the states of the target spacecraft in the Moon centered rotating frame, the position and the velocity of the chaser spacecraft with respect to the target and their relative orientation, orientation of the target in the inertial frame, as well as the instantaneous location of the approach site. In principle, the orientation of the target body relative to the Inertial frame as well as the instantaneous location of the approach site evolve independent (or decoupled) of the motion of the chaser spacecraft. As a consequence, pose observations do not affect the motion of the target body.

The Kalman filter processes the observed data while updating the covariance and estimates of the states within the stochastic system. To expedite the computational process, the Kalman filter is expressed in form of a linearized system of state equations near the baseline optimal path for the spacecraft motion. The equations are as formulated

$$\delta\mathbf{x}_{j+1} = \mathbf{A}_j\delta\mathbf{x}_j + \mathbf{B}_j\Delta\mathbf{v}_j + \mathbf{w}_j \quad [53]$$
$$\delta\mathbf{y}_{j+1} = \mathbf{H}_j\delta\mathbf{x}_j + \mathbf{e}_j \quad [54]$$

where measurement matrix, $\mathbf{H}_j = \frac{\partial\mathbf{y}}{\partial\mathbf{x}}$, whereas $\mathbf{w}_j$ and $\mathbf{e}_j$ are stochastic white noise with covariance $E[\mathbf{w}_j\mathbf{w}_j^{\mathrm{T}}] = \mathbb{Q}$ and $E[\mathbf{e}_j\mathbf{e}_j^{\mathrm{T}}] = \mathbb{R}$. Control inputs may are not delivered at the sampling frequency, therefore, the value for $\Delta\mathbf{v}_j$ may be zero at time t_j.

Filtering

The Kalman filter is based on the assumption that the noises, w_j and e_j, are Gaussian. Such an assumption is reasonable and delivers adequate results.[5] In principle, the sequential Kalman filter estimates the states and covariance by minimizing the mean square error of the estimated states from the reference. Each measurement is processed sequentially thus improving the computational time. The state estimates and the covariance are computed by

$$\delta\hat{\mathbf{x}}_{j|j} = \delta\hat{\mathbf{x}}_{j|j-1} + \mathbb{K}_j\delta\mathbf{y}_j \quad [55]$$
$$\mathbf{\Sigma}_{j|j} = \mathbf{\Sigma}_{j|j-1} - \mathbb{K}'_j\mathbf{H}_j\mathbf{\Sigma}_{j|j-1} \quad [56]$$
$$\mathbb{K}'_j = \mathbf{\Sigma}_{j,j-1}\mathbf{H}_j^T(\mathbf{H}_j\mathbf{\Sigma}_{j|j-1}\mathbf{H}_j^T + \mathbb{R})^{-1} \quad [57]$$
$$\mathbf{\Sigma}_{j+1|j} = \mathbf{A}_j\mathbf{\Sigma}_{j|j}\mathbf{A}_j^T + \mathbb{Q}_j \quad [58]$$

where $\delta\hat{\mathbf{x}}_{j|j-1}$ is the predicted estimate given $j-1$ observations are available, and $\delta\hat{\mathbf{x}}_{j|j}$ is the new estimate once the measurement at j-th observation is included. Kalman gain, $\mathbb{K}$, is a function of the system matrices, measurement covariance and state covariance. The quantity,

$$\mathbf{\Sigma}_{j|j-1} = E[(\delta\mathbf{x}_j - \delta\hat{\mathbf{x}}_{j|j-1})(\delta\mathbf{x}_j - \delta\hat{\mathbf{x}}_{j|j-1})^{\mathrm{T}}] \quad [59]$$

is the *a-priori* state covariance at the j-th interval once $j-1$ observations are recorded. Whereas, the covariance matrix

$$\mathbf{\Sigma}_{j|j} = E[(\delta\mathbf{x}_j - \delta\hat{\mathbf{x}}_{j|j})(\delta\mathbf{x}_j - \delta\hat{\mathbf{x}}_{j|j})^{\mathrm{T}}] \quad [60]$$

is the *a-posteriori* covariance calculated once the j-th observation is also incorporated. In the beginning, due to lack of prior observed data, the value for *a-priori* covariance $\mathbf{\Sigma}_{j|j-1}$ is set high. The covariance matrix is continuously updated as additional observations become available. Since the frequency for control maneuvers are smaller than the pose tracking data, there is enough time-span to capture sufficient observations and get reliable state estimates.

4.2 Linear Controller

A nonlinear controller is certainly more advanced and offer superior results than a linear controller, especially with the ability to evaluate complex set of nonlinear equations of motion: time-variant orbital dynamics and attitude dynamics of the system. Subsequently the nonlinear controller is preferred to identify suitable state and control history for close proximity operations. The computational expense for evaluating a nonlinear controller is substantially higher than that of a linear controller. A real time computation of the control maneuvers may be challenging. For the spacecraft to operate synchronously with any on-board software, controller must compute and deliver maneuvers at a pace faster than the actual clock time. Consequently, a nonlinear controller

is not adopted for the routine maneuver delivery process despite the benefits it offer. Alternatively, a relatively quicker linear controller is integrated with the nonlinear optimal controller to compute maneuvers for compensating any deviations detected from the predetermined baseline path. A linearized system is modeled using state-space representation for the dynamical flow in the neighborhood of the baseline path, analogous to the one described for the Kalman filter. The state transition matrices (or system matrices) are computed along the computed nonlinear baseline path, for each discrete control segment.

The benefits offered by both the nonlinear and the linear controller are exploited through a two-layered control approach. First and foremost, an ideal baseline rendezvous path is determined by the nonlinear controller, with a sequence of control outputs. In the absence of any perturbations or modelling error, the chaser spacecraft approaches the target spacecraft along the states of this baseline rendezvous path. The chaser spacecraft advances towards the target while incorporating the first control maneuver computed by the nonlinear controller. Pose observations are captured and offers feedback to the spacecraft motion. Subsequent maneuvers are determined by the linear controller to compensate any state deviations from the baseline path. Figure 3 offers a schematic of the linear controller used in conjunction with the nonlinear controller in this investigation. The baseline path represented in red is identified by the nonlinear controller while the green curve is symbolic of the true path. The state and control history along the baseline path is marked with an asterisk, $*$, whereas the state and control history without the asterisk denotes the true path. At initial time, t_0, the control output is $\mathbf{u}_0$; also $\mathbf{u}_0 = \mathbf{u}_0^*$. Subsequently the linear controller produces corrective maneuvers, $\delta\mathbf{u}_k$, at time t_k. The net control maneuver ($\mathbf{u}_k$) delivered to the chaser spacecraft is the total sum of the control outputs from the nonlinear ($\mathbf{u}_k^*$) and the linear controller ($\delta\mathbf{u}_k$), i.e., $\mathbf{u}_k = \mathbf{u}_k^* + \delta\mathbf{u}_k$. For convenience, the control outputs are maintained at the same frequency for the nonlinear and linear controllers. A summary of the rendezvous process exploiting a blended linear and nonlinear controller, along with state estimation and hardware simulations is presented in Fig. 4.

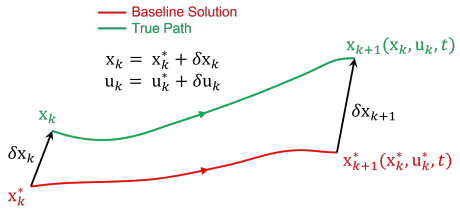

Fig. 3: Nonlinear control delivers a baseline/reference solution while linear controller compensates for any deviations from the baseline. The spacecraft advances along the true path.

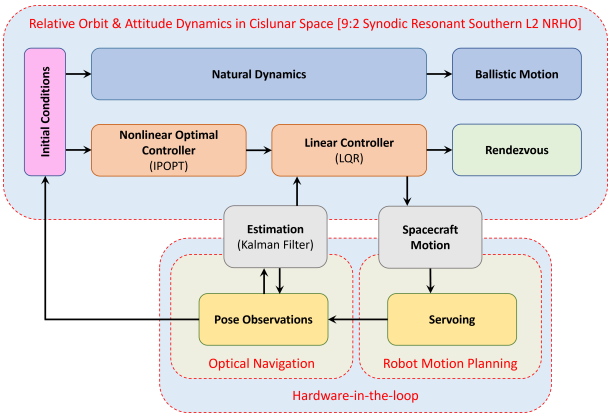

Fig. 4: Proximity operations flowchart: Control and estimation of spacecraft states.

System Dynamics

The orbit and attitude control is performed to overcome any perturbations that the spacecraft may have incurred due to limitations in navigational apparatus. A linear controller is adopted to rapidly deliver control maneuvers to compensate for any deviations measured from the baseline path, i.e., the quantity $\delta\mathbf{x}_k$. The uncertainties in state measurements are small, and hence, linear dynamics near the baseline path is sufficient to predict the appropriate control output. Based on the variational equations of motion computed near the reference path (one computed in section 3), the linear dynamics are governed by

$$\delta\mathbf{x}_{k+1} = \mathbf{A}_k\delta\mathbf{x}_k + \mathbf{B}_k\delta\mathbf{u}_k \qquad [61]$$

where $\mathbf{A}_k$ is the 29×29 state transition matrix, and $\mathbf{B}_k$ is a 29×6 matrix that corresponds to the partials of state vector at final time, $\mathbf{x}_{k+1}$, to a control vector $\delta\mathbf{u}_k$, evaluated along the baseline path. The motion of the target and the approach site are decoupled and independent from the motion of the chaser spacecraft, therefore, a number of partials within the matrix $\mathbf{A}_k$ are zeros, consequently making $\mathbf{A}_k$ a sparse matrix. Further, it is assumed that only the chaser spacecraft is controllable while the target has no control capabilities. The control inputs only affect the motion of the chaser spacecraft and do not affect the motion of the target body or the location of the approach site;

consequently, a number of partials within matrix $\mathbf{B}_k$ are zeros. The matrices $\mathbf{A}_k$ and $\mathbf{B}_k$ are computed numerically through central differencing technique.

Linear Quadratic Regulator (LQR)

Control outputs are delivered at discrete intervals using a discrete LQR controller. Once the system is linearized along the baseline solution, a feedback controller is formulated that minimizes the cost functional, $\tilde{J}$, such that

$$\tilde{J} = \delta\mathbf{x}_N^{\mathrm{T}}\tilde{\mathbf{P}}_N\delta\mathbf{x}_N + \sum_{k=0}^{N-1}\delta\mathbf{x}_k^{\mathrm{T}}\tilde{\mathbf{Q}}_k\delta\mathbf{x}_k + \delta\mathbf{u}_k^{\mathrm{T}}\tilde{\mathbf{R}}_k\delta\mathbf{u}_k \quad [62]$$

and penalizes on any deviations in state from the baseline path, as well as on the size of control. The solution to this LQR problem is given by,[15,16]

$$\delta\mathbf{u}_k = -\tilde{\mathbf{K}}_k\delta\mathbf{x}_k \quad [63]$$

where $\tilde{\mathbf{K}}_k$ is the time-dependent gain matrix that satisfies

$$\tilde{\mathbf{K}}_k = (\tilde{\mathbf{R}}_k + \mathbf{B}_k^{\mathrm{T}}\tilde{\mathbf{P}}_{k+1}\mathbf{B}_k)^{-1}\mathbf{B}_k^{\mathrm{T}}\tilde{\mathbf{P}}_{k+1}\mathbf{A}_k \quad [64]$$

and $\tilde{\mathbf{P}}_k$ satisfies the discrete algebraic Riccati equation,

$$\tilde{\mathbf{P}}_k = \tilde{\mathbf{Q}}_k + \mathbf{A}_k^{\mathrm{T}}\tilde{\mathbf{P}}_{k+1}\mathbf{A}_k - \mathbf{A}_k^{\mathrm{T}}\tilde{\mathbf{P}}_{k+1}\mathbf{B}_k\tilde{\mathbf{K}}_k \quad [65]$$

for $k = 0, \ldots, N-1$. Each of $\tilde{\mathbf{Q}}_k$ and $\tilde{\mathbf{R}}_k$ are positive definite weighting matrices or penalty matrices. The quantity N is the total number of discrete segments of the approach path considered for proximity operations.

Control maneuvers are delivered at a lower frequency than that of the state estimation using Kalman filter. Pose values are passed through the Kalman filter at a significantly higher frequency to refine measurements and get an estimate void of large fluctuations. Also, two successive control outputs (maneuvers) must be placed sufficiently apart for the proper estimation of the spacecraft's position, velocity and orientation states with sufficient precision. A schematic representation of the process (observations, estimation and control) timeline is presented in Fig. 5. As mentioned, high-frequency pose observations are symbolized by magenta dots. Larger red dots correspond to discrete intervals at which control maneuvers are identified by the nonlinear optimal control algorithm. The red curve acts as the baseline for the proximity operations. True spacecraft path is illustrated by the Green curve in Fig. 5, one that incorporates deviations due to uncertainties in state measurements; consequently, it does not precisely overlap the red curve rather remains in the neighborhood of the baseline path. The gray dotted curve is the updated estimated path as the observed data is processed through the Kalman filter. Finally, a solid blue curve reflects the ballistic motion in the absence of any control maneuvers.

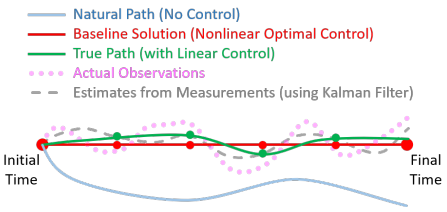

Fig. 5: Time history of natural path, optimal path for rendezvous and true path. Red and green dots correspond to intervals of control outputs, while magenta dots corresponds to the intervals for pose observations recorded by the optical sensors.

5. Results

The final approach phase is considered for evaluating the proximity operations in this investigation. When the distance between the chaser and the target is considerably large, the effects of the relative orientation is less significant. The controller is biased towards determining an optimal trajectory for the chaser to approach the target spacecraft. In contrast, when the relative distance between the chaser and the target is small, a similar emphasis is allotted for determining a rendezvous trajectory as well as maintaining appropriate relative orientation between the chaser and target spacecrafts. Such a scenario is effective for testing and validating the control algorithm for proximity operations. Test cases are evaluated considering the target spacecraft, such as the Gateway, to be located at the apoapsis of the 9:2 synodic resonant southern NRHO at the start of the rendezvous operations. Also, the target spacecraft is considered to be passive with no attitude control. Furthermore, the target is deliberately treated as tumbling under the influence of gravity torques exerted by the Earth and the Moon to further test the potency of the control algorithm. Consequently, a complex rendezvous scenario involving a non-cooperative and tumbling target is induced. In this investigation two types of tests are presented: (1) testing the controller performance based on simulation and (2) hardware-in-the-loop (HITL) tests as a proof-of-concept for rendezvous in cislunar space with

navigation using ArUco markers based optical sensing. The target and chaser spacecrafts are modelled as uniform density 6U CubeSats. The control algorithm is programmed in Python while the interface with robotic manipulators and visual pose estimations are achieved over the Robot Operating System (ROS) network.

5.1 Controller Performance

The final approach phase for the spacecrafts are considered in this investigation where the trajectory and the orientation of both the chaser and target spacecrafts are relevant. Of course the control algorithm does not vary depending on the distance of separation between the two spacecrafts in picture. Two distinct and diverse cases are examined to test the capabilities of the control algorithm. The parameters used for these cases are documented in Table 1. In case 1, the initial separation distance between the chaser and the target spacecraft is roughly 3.8 m and the proximity operations happen in a duration of 4 hours. For case 2, initial separation distance is roughly 40 m, i.e., an order of magnitude larger than case 1. Furthermore, the rendezvous operations in case 2 happen within 3 hours; faster than case 1. About 120 equally-spaced control inputs are delivered over the course in case 1 while only 60 control maneuvers are delivered in case 2. The maximum control acceleration and torque values are within the proposed values for the Gateway mission.[17] Different weights used for evaluating the cost functional and to determine an optimal rendezvous path are as listed in Table 1 for both the cases.

Table 1: Sample parameters for testing controller performance.

	Case 1	Case 2
Initial separation in LVLH frame ([x,y,z] m)	[-3.5, 1.5, 0]	[35,-15,-10]
Distance at rendezvous [m]	0.6	2
Collision avoidance distance [m]	0.6	2
Total time of propagation [hr]	4	3
Control segments	120	60
Max. control acceleration [m/s^2]	1.1×10^{-6}	2.7×10^{-5}
Max. control torque per kg [Nm]	1.4×10^{-9}	7.0×10^{-8}
$\mathbf{Q}_1$ [diagonal in $\log_{10}$ scale]	[3, 3, 3]	[0, 0, 0]
$\mathbf{Q}_2$ [diagonal in $\log_{10}$ scale]	[1, 1, 1]	[1, 1, 1]
$\mathbf{Q}_3$ [diagonal in $\log_{10}$ scale]	[0, 0, 0]	[0, 0, 0]
$\mathbf{R}$ [diagonal in $\log_{10}$ scale]	$[-1, -1, -1, -2, -2, -2]$	[0, 0, 0, -2, -2, -2]
Pose observation interval [s]	30	30
Errors in pose (3σ)	15 cm in x,y,z (absolute error) 0.03 in ϵ_i	10% in x,y,z (relative error) 0.03 in ϵ_i
Incorrect orientation or pose flipping	1 in 30 observations	1 in 30 observations

Effects of uncertainties in pose estimation has an adverse effect on the costs required to maintain the chaser spacecraft along the determined rendezvous path. The effects of uncertainties in pose identification on the control costs are tested by synthetically introducing perturbations in the position and orientation components and calculating the values of $\delta\mathbf{u}_k$. For both the cases, observations are assumed to be available once every 30 seconds, and 1 in every 30 observations are considered to be pose flipped or supplying incorrect orientation values. Furthermore, in case 1, the position components along each directions are perturbed by an absolute 3σ value of 15 cms. In contrast, a 3σ relative position error of 10% in introduced in each of the three spatial directions. The orientation quaternions are perturbed by a 3σ value of 0.03 along each components, for both the cases.

A reference rendezvous path in case 1 is identified with the approach cite at 0.6 m from the center of the target spacecraft; consequently, collision avoidance distance is set to 0.6 m. The optimal path in the configuration space is demonstrated in Fig. 6. Orientation of the target and chaser at a certain time instance is also plotted to describe their mutual identical orientation during the rendezvous process. Since the Kalman filter compensates for fluctuations

in pose observations, distinct behavior is not observed at a macro level between the two paths. However, by investigating the evolution of the position coordinates in Fig. 7, a clear distinction is observed between the reference path, the true path of spacecraft motion and the estimated derived from the routine pose observations. Finally, acceleration and torque control history for the proximity operations in case 1 are delivered in Fig. 8. Again, note that the optimal maneuvers are determined by the nonlinear controller while the actual maneuvers that are delivered include corrective maneuvers to compensate for any deviations from the reference path that are identified by routine pose observations.

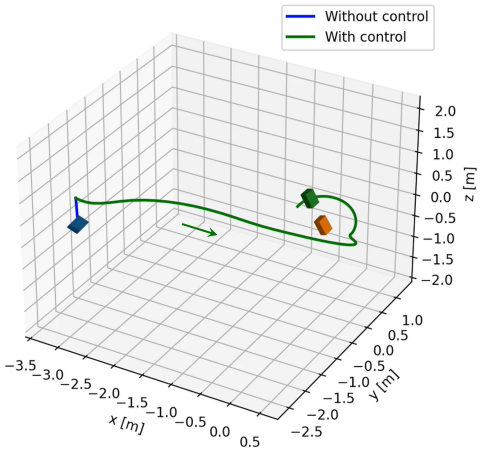

Fig. 6: Optimal path for rendezvous, with a sample orientation of target and chaser spacecraft. Frame: LVLH. Target is colored orange. CubeSat scale: 2X. (Case 1)

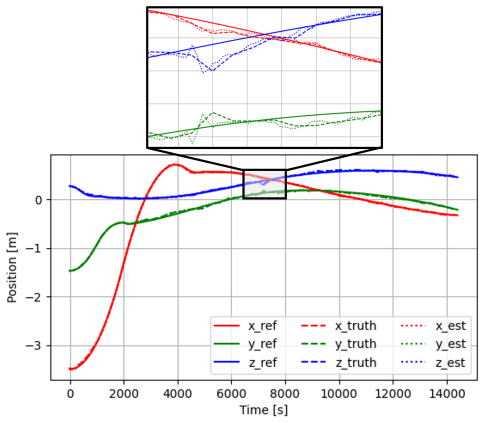

Fig. 7: Position state history for the proximity operations. (Case 1)

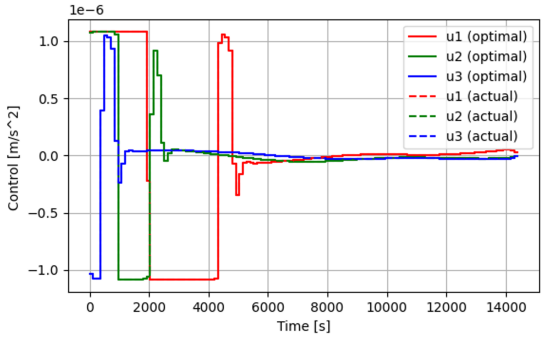

(a) Acceleration control history

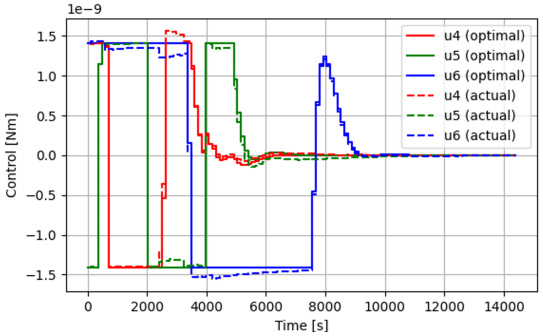

(b) Torque control history

Fig. 8: Control history for rendezvous operations. (Case 1)

Similarly for case 2, a reference rendezvous path is identified with the approach cite at 2 m from the center of the target spacecraft; the collision avoidance distance is also set to 2 m. The optimal path in the configuration space along with a sample orientation of the two spacecrafts are demonstrated in Fig. 9. The evolution of the position coordinates are plotted in Fig. 10, for the reference path, the true path of spacecraft motion and the estimated path. The acceleration and torque control history for case 2 are shown in Fig. 11. In contrast to case 1, the maximum acceleration and torque level (along the reference path computed by nonlinear optimal control) is higher in case 2, offering a rapid progression of the chaser towards the approach site near the target spacecraft. Consequently, the magnitude of control inputs are higher initially, and reduces considerably with time.

Irrespective of the cases investigated, it is observed that poor pose observations increase uncertainties in state estimation, eventually resulting in increased deviations from the baseline path; consequently, driving the control costs higher. Frequent and precise state

observations are key to reducing magnitude of corrective maneuvers.

5.2 Hardware-in-the-loop tests

Autonomy of the control algorithm for rendezvous operations is validated using hardware-in-the-loop tests. These tests are proof-of-concept for guidance and control strategies leveraging optical navigation techniques. Such autonomy presents potential opportunities in cislunar missions. The guidance, navigation and control (GNC) techniques are validated in a sophisticated test facility.

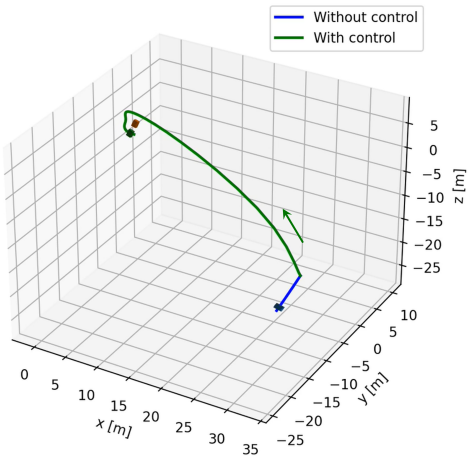

Fig. 9: Optimal path for rendezvous, with a sample orientation of target and chaser spacecraft. Frame: LVLH. Target is colored orange. CubeSat scale: 4X. (Case 2)

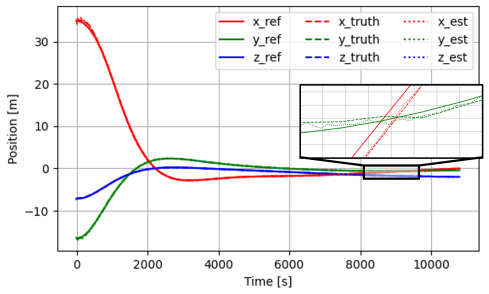

Fig. 10: Position state history for the proximity operations. (Case 2)

Experimental setup

The ZeroG Lab at the University of Luxembourg is a robotic test facility for real-time simulation of on-orbit servicing missions. As demonstrated in Fig. 12, the facility is a 5m x 3m area. The facility has four

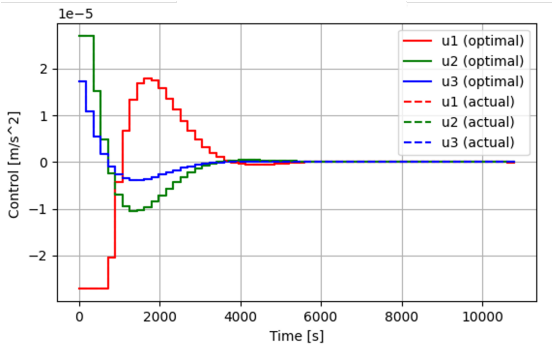

(a) Acceleration control history

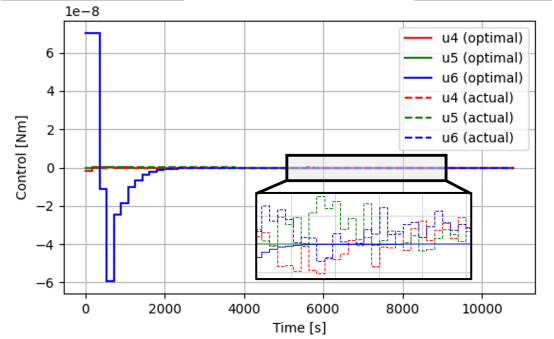

(b) Torque control history

Fig. 11: Control history for rendezvous operations. (Case 2)

main components to emulate on-orbit scenarios: a Sun emulator to recreate the challenging space lighting conditions, a 240 Hz advanced Motion Capture System (MCS) to provide ground truth data, and two UR10e robotic manipulators. Each robotic manipulator has six degree-of-freedom and is mounted on a rail to provide an additional range of motion suitable for simulating spacecraft motion in on-orbital scenarios. The UR10e robots, the MCS as well as other external devices communicate using the Robot Operating System (ROS). External commands to control these robotic manipulators are also directed over the ROS network. A mock-up of the target spacecraft is mounted on the ceiling arm's flange. Likewise, the mock-up simulating the chaser spacecraft, in form of an optical camera, is mounted on the wall robotic arm. It is possible to provide the rendezvous path in the form of Cartesian set-points. These paths are updated based on visual feedback and pose estimation, while servoing is performed to guide the chaser spacecraft to approach the target in the position space, as well as follow any changes in the orientation of the target.

Relative state estimation in proximity operations

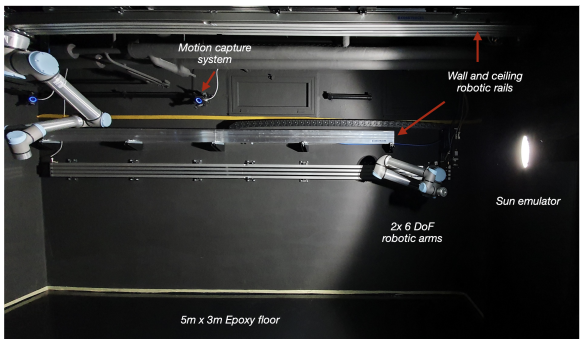

Fig. 12: The ZeroG lab facility at University of Luxembourg.

is supported by visual observations of the pre-defined passive fiducial marker array used on the target spacecraft. To emulate this, an Intel Realsense D435i camera is mounted on the wall robotic arm located on the right that emulates the chaser spacecraft. Owing to their superior balance of performance, speed, and detection reliability, ArUco[18,19] markers are glued on the target spacecraft mock-up. Unique detection of each ArUco marker is facilitated by its encoding dictionary,[20] which provides a unique combination of $n_e x n_e$ array of bits that take a binary value. The ArUco markers provide reasonably precise localization of the four corners that enclose them. Once the locations of marker corners are obtained, the pose of the known body frame relative to the camera is estimated using the Perspective-n-Points formulation, given the knowledge of the target's 3D wireframe model, the intrinsic parameters of the observing camera, and the 2D location of the feature in the image. Figure 13 illustrates the detection of seven ArUco markers mounted on the mock-up of the target spacecraft.

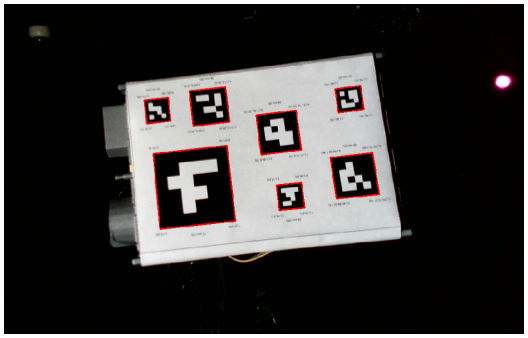

Fig. 13: ArUco markers on CubeSat mock-up identified for pose estimation.

The HITL experiments are conducted in the ZeroG lab with the Sun emulator as the only light source for an increased fidelity in simulating the space environment. RViz is a ROS graphical interface that enables visualization of several ROS topics and assists in remote documentation and monitoring of the experiments. Figure 14 presents RViz with the actual robot configuration, visual feedback from the camera with the detection of ArUco markers on the target spacecraft, and visualization of the static transformations.

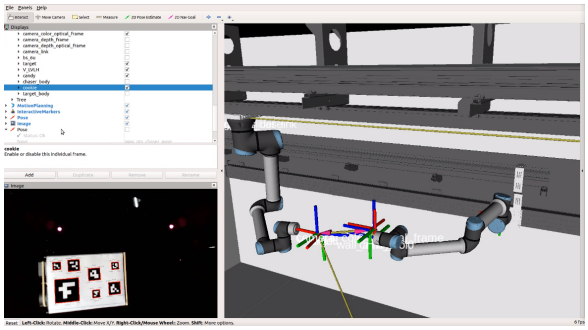

Fig. 14: Robot motion planning interface as visualized on RViz toolkit.

Hardware-in-the-Loop results

The rendezvous path is constrained to lie within the limited workspace accessible to the robotic arms as well as the marker detection distance for the camera. Initial conditions for the proximity operations are identified from the pre-existing configuration of both the robotic arms within their accessible workspace; an initial separation of approximately 0.8m was determined. The relative pose of the target spacecraft is determined and an optimal path is calculated; the one determined in the experiment for a rendezvous duration of 3 hours is plotted in Fig. 15. A sequence of 120 control segments are thus placed at segment intervals of 90 seconds. Pose observations are recorded once every 5 seconds. Deviations caused as a result of uncertainties in the pose are compensated with regular corrective maneuvers. The control history for the setup is presented in Fig. 16. Determination of the pose of a moving target while the chaser itself is in motion, changing lighting conditions, the direction of the optical camera, and separation distance between the chaser and target induce fluctuations in pose values. Despite these fluctuations, the chaser is able to rendezvous with the target in the neighborhood of the determined reference path. The functionality of the control algorithm to perform in sync with the pose estimation algorithm and robotic

manipulators (for emulating actual spacecraft trajectory) is validated with the HITL tests. Furthermore, real-time pose estimation for spacecraft navigation presents opportunities for precise rendezvous. Improved algorithms for a wider range of pose estimation potentially overcome the existing challenge of a limited operating distance of separation between spacecraft.

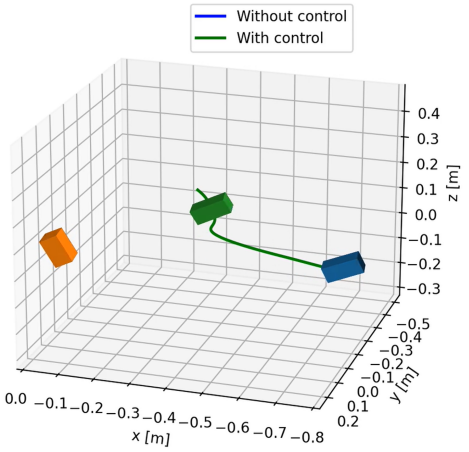

Fig. 15: Optimal path for rendezvous, determined for HITL experiments. Sample orientation of target and chaser spacecraft at illustrated. Frame: LVLH. Target is colored orange. CubeSat scale: 0.6X.

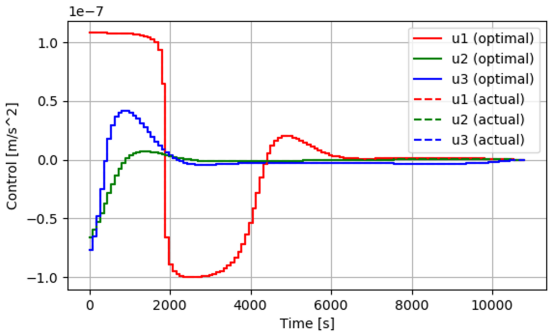

(a) Acceleration control history

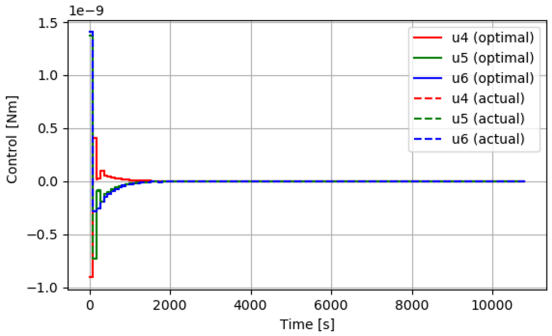

(b) Torque control history

Fig. 16: Control history for experimental rendezvous operations

6. Concluding Remarks

This investigation presents a GNC technique for autonomous proximity operations in the cislunar space. A two-layered control approach is adopted. Firstly, a nonlinear controller is designed that accounts for both orbit and attitude motion for the chaser and target spacecrafts in the circular restricted three-body problem. Further, the linear controller compensates for any deviations from the predetermined path, with feedback obtained from optical pose estimations. The designed controller is capable of performing rendezvous with a wide range of separations; two distinct cases are presented to validate the ability. The control algorithm is capable of rendezvous operations with an even larger distance of separation between the spacecrafts; weighting matrices of cost functional may be altered on a case-by-case basis. A proof-of-concept autonomous GNC technique is presented with hardware-in-the-loop experiments, wherein the two robots emulate the motion of the chaser and target spacecrafts for rendezvous in an NRHO. Real-time pose observations with frequent readings offer precise feedback for state estimates even with few pose flipping/incorrect poses; therefore, adequate for delivering corrective maneuvers. The success of the hardware-in-the-loop experiment further offers opportunities for evaluating algorithms for long-range pose estimation, challenging lighting conditions, and a wider range of robot motion to emulate spacecraft paths. The advancements in the GNC algorithm to actively support rendezvous operation with onboard optical navigation equipment enables exploitation of such operations in regions inaccessible directly from the Earth, for example, away from the line of sight from the Earth. Such techniques further augment the capability to conduct rendezvous in deep space, significantly farther from Earth.

References

[1] Sean Fuller, Emma Lehnhardt, Christina Zaid, and Kate Halloran. Gateway program status and overview. In *72nd International Astronautical Congress, Dubai, UAE*, 2021.

[2] Jason Crusan, Jacob Bleacher, Joe Caram, Dou-

glas Craig, Kandyce Goodliff, Nicole Herrmann, Erin Mahoney, and Marshall Smith. Nasa's gateway: an update on progress and plans for extending human presence to cislunar space. In *IEEE Aerospace Conference*, pages 1–19, 2019.

[3] Davide Guzzetti and Kathleen C. Howell. Coupled orbit-attitude dynamics in the three-body problem: A family of orbit-attitude periodic solutions. In *AIAA/AAS Astrodynamics Specialist Conference, San Diego, California, USA*, 2014.

[4] Vivek Muralidharan, Carol Martinez Luna, Augustinas Zinys, Marius Klimavicius, and Miguel Angel Olivares Mendez. Autonomous control for satellite rendezvous in near-earth orbits. In *International Conference on Control, Automation and Diagnosis (ICCAD'22), Lisbon, Portugal*. IEEE, 2022.

[5] Vivek Muralidharan, Avishai Weiss, and Uros V Kalabic. Control Strategy for Long-Term Station-Keeping on Near-Rectilinear Halo Orbits. In *30th AIAA/AAS Space Flight Mechanics Meeting, Orlando, FL, USA*, January 2020.

[6] Victor Szebehely. Theory of orbits: the restricted problem of three bodies. Technical report, Yale University, New Haven, Connecticut, USA, 1967.

[7] Vivek Muralidharan and Kathleen C. Howell. Leveraging stretching directions for stationkeeping in earth-moon halo orbits. *Advances in Space Research*, 69(1):620–646, 2022.

[8] James R Wertz and Robert Bell. Autonomous rendezvous and docking technologies: status and prospects. *Space Systems Technology and Operations*, 5088:20–30, 2003.

[9] Fouad Khoury and Kathleen C. Howell. Orbital rendezvous and spacecraft loitering in the earth-moon system. In *AAS/AIAA Astrodynamics Specialist Conference, Lake Tahoe, California, USA*, 2020.

[10] Giovanni Franzini and Mario Innocenti. Relative motion equations in the local-vertical local-horizon frame for rendezvous in lunar orbits. In *AAS/AIAA Astrodynamics Specialist Conference, Stevenson, WA, USA*, 2017.

[11] Andrea Colagrossi, Vincenzo Pesce, Lorenzo Bucci, Francesco Colombi, and Michèle Lavagna. Guidance, navigation and control for 6dof rendezvous in cislunar multi-body environment. *Aerospace Science and Technology*, 114:106751, 2021.

[12] Davide Guzzetti and Kathleen C. Howell. Attitude dynamics in the circular restricted three-body problem. *Astrodynamics*, 2(2):87–119, 2018.

[13] Joel A E Andersson, Joris Gillis, Greg Horn, James B Rawlings, and Moritz Diehl. CasADi – A software framework for nonlinear optimization and optimal control. *Mathematical Programming Computation*, 11(1):1–36, 2019.

[14] Oliver Montenbruck, Eberhard Gill, and Fh Lutze. Satellite orbits: models, methods, and applications. *Appl. Mech. Rev.*, 55(2):B27–B28, 2002.

[15] R. F. Stengel. *Optimal Control and Estimation*. Courier Corporation, 1994.

[16] Vivek Muralidharan, Avishai Weiss, and Uros Kalabic. Tracking neighboring quasi-satellite orbits around Phobos. In *World Congress of the International Federation of Automatic Control (IFAC), Berlin, Germany*, page 14906–14911. Elsevier, 2020.

[17] Robert Pritchett, Kathleen C. Howell, and David C Folta. Low-thrust trajectory design for a cislunar cubesat leveraging structures from the bicircular restricted four-body problem. In *International Astronautical Congress, Washington D.C., USA*, 2019.

[18] Sergio Garrido-Jurado, Rafael Muñoz-Salinas, Francisco José Madrid-Cuevas, and Manuel Jesús Marín-Jiménez. Automatic generation and detection of highly reliable fiducial markers under occlusion. *Pattern Recognit.*, 47(6):2280–2292, 2014.

[19] Francisco J. Romero Ramírez, Rafael Muñoz-Salinas, and Rafael Medina Carnicer. Speeded up detection of squared fiducial markers. *Image Vis. Comput.*, 76:38–47, 2018.

[20] Sergio Garrido-Jurado, Rafael Muñoz-Salinas, Francisco José Madrid-Cuevas, and Rafael Medina Carnicer. Generation of fiducial marker dictionaries using mixed integer linear programming. *Pattern Recognit.*, 51:481–491, 2016.